The Effect of SnO$_2$ Surface Properties on CO$_2$ Photoreduction to Higher Hydrocarbons

Juliana A. Torres,[a] André E. Nogueira,[b] Gelson T. S. T. da Silva,[a] and Caue Ribeiro*[a]

Several photocatalysts have been developed for applications in reduction reactions, including tin oxide-based semiconductors. Although its band structure is unfavorable for CO$_2$ reduction reactions, strategies to modify its surface properties directly impacted its activity and selectivity during these reactions. Here, we analyze the influence of heat treatment and decoration of SnO$_2$ with gold nanoparticles on the gas phase CO$_2$ photoreduction process. In both cases, a deleterious effect was observed during reactions under UV radiation (with a drop of 59.81% and 51.45% in CH$_4$ production for SnO$_2$_150°C and SnO$_2$/Au_cop, respectively, compared to SnO$_2$_cop), which is directly related to the availability of surface hydroxyl groups that play a crucial role in CO$_2$ adsorption. Under visible radiation, the gold plasmonic resonance took place in the production of methane (0.33 μmol g^{-1} for SnO$_2$/Au_cop and 0.29 μmol g^{-1} for SnO$_2$/Au_150°C), with small amounts of carbon monoxide (0.06 μmol g^{-1} for SnO$_2$/Au_cop and 0.03 μmol g^{-1} for SnO$_2$/Au_150°C). These results demonstrate that, though the SnO$_2$ band structure does not indicate a good semiconductor for CO$_2$ reduction, its surface characteristics are responsible for its catalytic activity.

Introduction

Several projections, such as in the COP26 final document (Glasgow Climate Pact 2021), show that emissions in 2030 will be almost 14% compared to 2010 unless new policies move towards reducing the carbon dioxide (CO$_2$) amount in the atmosphere. In addition, the document shows that it will be necessary to reduce CO$_2$ emissions by 45% by 2030 at about 2010 levels to keep global warming at 1.5°C above pre-industrial levels.[1] For 2050–2070, the goals set out are even more ambitious. The aim is to achieve an energy network with a neutral carbon balance by implementing the principles of a circular economy compatible with existing industrial technologies.[2] In this way, there will be a continuous search for new technologies to meet this global demand.

A more sustainable alternative to the capture and storage of CO$_2$ would be CO$_2$ utilization for fuel or chemical production. Converting CO$_2$ into other products not only eliminates the costs associated with transport and storage, which typically represent between 35% and 40% of the total cost of products,[3] but also transforms waste into sources of income through the production of compounds of economic interest,

such as methane, ethylene, carbon monoxide, and ethane, among others.

Different processes can carry out the CO$_2$ conversion into products with higher energy values, such as thermal,[4] electrochemical,[5] photo-electrochemical,[6] and photocatalytic processes,[7] in which they differ by the type of energy used to reduce the CO$_2$ molecule. The great interest in photocatalytic processes is due to their simplicity. The reactions occur at room temperature and pressure with a low energy cost due to the possibility of using solar radiation and semiconductors as catalysts.

CO$_2$ photoreduction is based on the principles of photosynthesis, in which, through the absorption of an external energy source by a semiconductor, CO$_2$ can be reduced to value-added products or fuel-based products. In this process, the CO$_2$ molecule is adsorbed on the catalyst surface, activated, and transformed into different intermediates. At the end, CO$_2$ reduction products are desorbed and released. It can be described as a multi-electronic process, in which electrons and holes (e^-/h^+) are produced on the photocatalyst surface from energy absorption. In this way, photocatalysis is an environmentally friendly alternative to convert CO$_2$ into different products of economic interest such as CO, HCOOH, CH$_3$OH, CH$_4$ and higher alkanes and alkenes.[8–11]

Due to some properties as good chemical stability, non-toxicity, low cost, and high electron mobility (240 cm^2/V·s), tin dioxide (SnO$_2$) has been identified as a promising semiconductor for photocatalytic process applications.[12] Sn-modified materials are widely used in different applications, including biomass conversion,[13,14] solar cells,[15–17] as solid-state chemical sensors,[18–20] and in high-capacity lithium-storage devices.[21–23] On the other hand, SnO$_2$'s use as a photocatalyst in the CO$_2$ photoreduction process is constrained by its high theoretical reduction potential in the conduction band (E° = ~0.5 V, V vs. NHE, pH 7). Since the photogenerated electrons in the reaction

[a] *Dra. J. A. Torres, Dr. G. T. S. T. da Silva, Dr. C. Ribeiro*
Nanotechnology National Laboratory for Agriculture (LNNA)
Embrapa Instrumentation
Rua XV de Novembro, 1452
CEP 13560-970, São Carlos/SP (Brazil)
E-mail: caue.ribeiro@embrapa.com.br
[b] *Dr. A. E. Nogueira*
Department of Chemistry
Federal University of Ouro Preto (UFOP)
Rua Diogo de Vasconcelos, 122
CEP 35400-000, Ouro Preto/MG (Brazil)

🖳 Supporting information for this article is available on the WWW under https://doi.org/10.1002/cctc.202201534

This publication is part of "Catalysis in Latin America". Please check the ChemCatChem homepage for more articles in the collection.

ChemCatChem

Research Article
doi.org/10.1002/cctc.202201534

Chemistry Europe
European Chemical
Societies Publishing

system should be transferred to the CO_2 molecule, it won't happen if the reduction potential of the semiconductor conduction band (CB) is less than the reduction potential, for example, from the conversion of CO_2 to methane ($CH_4 = E°$ (CO_2/CH_4) $= -0,24$ V).[24,25]

However, Chowdhury et al. experimentally verified the ability to convert CO_2 to formic acid (HCOOH) using mesoporous SnO_2 nanoparticles in photocatalysis in aqueous media under ultraviolet radiation (UV) and visible radiation.[26] In addition, preliminary studies by our research group experimentally verified the activity of SnO_2 nanoparticles in the CO_2 photoreduction process, converting CO_2 into CH_4, carbon monoxide (CO), and ethylene, showing that surface hydroxyls played a crucial role in the photocatalytic activity of the semiconductor, in which these groups increased CO_2 affinity and possibly decreased its reduction potential.[27]

Several strategies are currently being adopted to modify the SnO_2 surface to increase the photocatalytic activity (both in oxidation and reduction systems), such as forming heterostructures, decoration with metals, or doping.[28] In this way, we propose a study of the physicochemical properties of pristine SnO_2, compared with SnO_2 decorated with gold nanoparticles, to correlate their properties with activity and selectivity in the CO_2 photoreduction process under UV and visible radiation.

Results and Discussion

Characterization

The X-ray diffraction pattern (XRD) of SnO_2_cop, SnO_2/Au_cop, and the calcined samples at 150 °C are shown in Figure 1. The tetragonal cassiterite phase profile (JCPDS N° 41–1445) is seen for all patterns, with the characteristic planes highlighted.[29,30] As predicted by Scherrer's equation, low intensity and broad
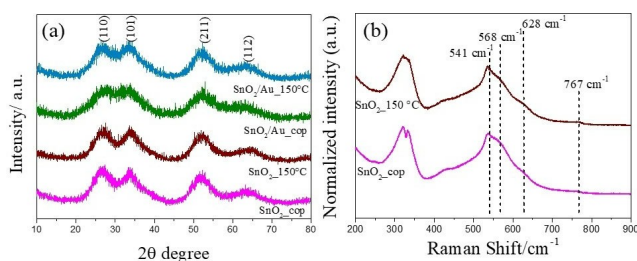
diffraction peaks are peculiar to small particle sizes.[25,31] The average crystallite size for SnO_2_cop is 1.50 nm, while for SnO_2_150 °C, it is 1.73 nm (Table 1). The gold diffraction peaks were not observed, probably due to the small amount.

Raman spectroscopy was used to understand the surface characteristics of SnO_2 that can directly influence its catalytic activity. Figure 1b shows the spectra of pristine and calcined SnO_2, while the samples containing gold did not show Raman-active modes.

The symmetric A_{1g} and asymmetric B_{2g} classical vibration modes, respectively, correspond to bands in the rutile tetragonal phase SnO_2 at about 628 and 767 cm^{-1}.[32] A result of the crystal's structural irregularity are bands at about 541 and 568 cm^{-1}.[33] Bridging, sub-bridging, and in-plane oxygen vacancies are three different forms of oxygen vacancies that can be studied using Raman spectroscopy. For example, the peak identified around 570 cm^{-1} is due to oxygen vacancies in the plane.[29,34] Once more, the SnO_2 surface vacancies are crucial to the catalytic activity of these materials.

Additionally, the sizes of nanoparticles are directly related to the classical modes of Raman vibration. As particle size approaches the nanoscale range, there is a relaxation of selection rules, causing the Raman bands broadening, turn down the intensity, and red shifting. In this way, the environment around the surface atoms in nanometric crystals affects them, changing the vibrational modes that may be seen in the Raman spectrum.[33,35,36] A typical example is at 200–400 cm^{-1} in Figure 1b.

X-ray fluorescence (XRF) technique was used to determine the gold content at the SnO_2 surface. The results are within the expected range (Table 1), indicating that the synthesis method used was adequate to produce gold nanoparticles on the SnO_2 surface.

The band structure of a photocatalyst is one of the crucial parameters that determine its photocatalytic activity. It is known that SnO_2 has a high bandgap (~ 3.6 eV) and a conduction band position that does not favor its application in reduction reactions.[30,37–39] In this sense, the determination of the bandgap is essentially important to understand the optical properties of these materials, as well as to verify the influence of gold nanoparticles in the energy absorption process. All materials displayed absorption in the ultraviolet range of the electromagnetic spectrum (below 400 nm), as predicted for SnO_2. The bandgap remained practically the same after SnO_2 decoration with gold (Table 1) and calcination (Figure S4).

Figure 2 shows that while all samples exhibit substantial ultraviolet absorption (up to 400 nm) due to surface plasmon
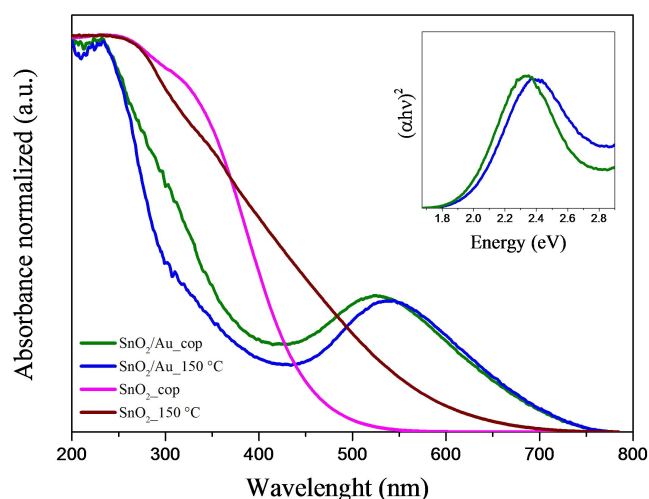

Figure 1. XRD pattern (a) and Raman spectra of the SnO_2 pristine and $SnO_2/$Au calcined at 150 °C (b).

Table 1. Bandgap energy, gold content (by XRF), FHWM, and the samples' average crystallite size (D-Scherrer).

Material	Bandgap [eV]	Au [wt%]	2θ [degree][a]	FWHM [rad]	D-Scherrer [nm])
SnO_2_cop	4.06	–	52.06	0.0934	1.50
SnO_2_150 °C	4.23	–	52.19	0.0811	1.73
SnO_2/Au_cop	4.14	1.11	52.53	0.1190	1.18
SnO_2/Au_150 °C	4.18	1.03	52.38	0.0990	1.42

[a] Bragg angles (2θ) were used to determine the FWHM and average crystallite size.

ChemCatChem

Research Article
doi.org/10.1002/cctc.202201534

Chemistry
Europe
European Chemical
Societies Publishing

Figure 2. UV-Vis DRS of the gold-impregnated samples. Inset graph: Tauc plots.

Figure 3. HRTEM images (a) SnO$_2$_cop, (b) SnO$_2$_150 °C, (d) SnO$_2$/Au_cop, and (f) SnO$_2$/Au_150 °C, and TEM images (c) SnO$_2$/Au_cop and (e) SnO$_2$/Au_150 °C.

resonance, which is a fundamental property of coinage metals (Au, Ag, and Cu), samples containing gold nanoparticles have an absorption peak at about 550 nm.[40–42]

SEM images show that pristine SnO$_2$ and SnO$_2$ with gold nanoparticles before and after calcination form agglomerates of irregular nanoparticles without significant variations in morphology between samples (Figure S2). Elemental mapping of SnO$_2$/Au_150 °C was carried out to prove the presence of gold on the SnO$_2$ surface. The presence of gold nanoparticles can be identified in the line scan profile (Figure S3a) and the delimited region profile (Figure S3b). Through the HRTEM images (Figure 3), it was possible to determine the characteristic lattice spacing of SnO$_2$ and gold nanoparticles, and to prove the presence of gold on the SnO$_2$ surface, corroborating the other results obtained. It is observed that the SnO$_2$ nanoparticles form quasi-spherical agglomerates of approximately 5 nm (Figure 3a and 3b), with a lattice spacing of 0.34 nm, referring to the (110) plane.[29,43] In the bright field image of SnO$_2$/Au_cop (Figure 3c), the scattered dark spots are the gold spherical nanoparticles, which are easily identified, while in the dark field image of SnO$_2$/Au_150 °C (Figure 3e), the gold nanoparticles are identified by the scattered bright spots, mainly at the edge of the SnO$_2$. Since Au has a higher mass-thickness contrast than Sn and O, its identification is easily performed in this image. The HRTEM images (Figure 3d and 3f) indicate that the gold spherical nanoparticles have a size of approximately 5 nm, with a lattice spacing of 0.24 nm, referring to the (111) plane.[40,42,44,45]

Using the XPS technique, the surface chemical composition and elemental valence state of SnO$_2$ and SnO$_2$/Au nanocomposite were examined (Figure 4). The benchmark for XPS peak correction is the 284.6 eV binding energy for the C 1s peak.[46] The XPS survey spectrum shows the presence of three elements: oxygen (O), carbon (C), and tin (Sn) in all materials, and no traces of impurities were observed. However, in the survey scan XPS spectra of SnO$_2$/Au_150 °C, we can notice a small peak related to gold (Au).
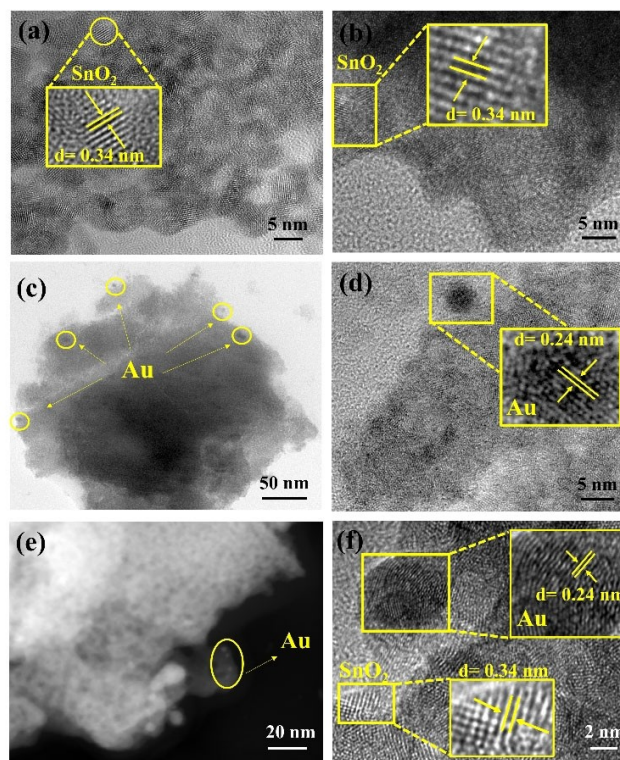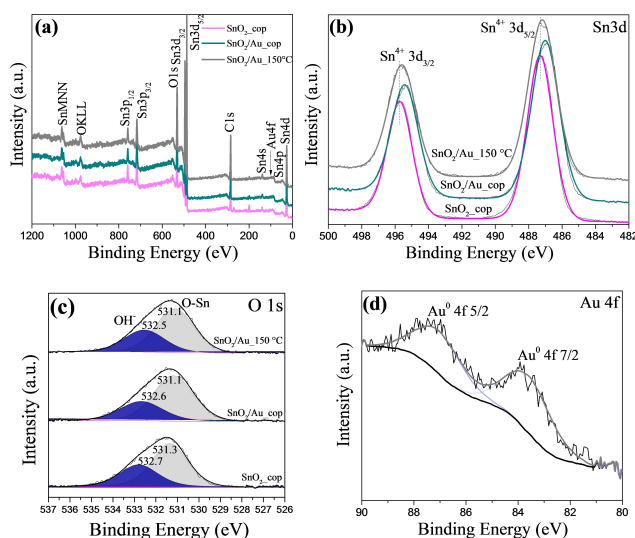

Figure 4. XPS survey spectra (a), and Sn3d (b), O1s (c), and Au4f (d) high-resolution XPS spectra of the materials SnO$_2$_cop, SnO$_2$/Au_cop, and SnO$_2$/Au_150 °C.

In the Sn3d spectrum of SnO$_2$_cop, the presence of two peaks at 487.3 eV and 495.7 eV related to the oxidation state of Sn^{4+} in SnO$_2$ is observed (Figure 4b). After the incorporation of gold nanoparticles, there is a slight shift of these peaks to less binding energy, attributed to the electronic interaction between

ChemCatChem

Research Article
doi.org/10.1002/cctc.202201534

**Chemistry
Europe**

European Chemical
Societies Publishing

Au nanoparticles and SnO_2. However, in accordance with the literature,[47] the distance between the Sn 3d3/2 and Sn 3d5/2 peaks, that is, the spin-orbit division, remains constant (8.4 eV). The high-resolution O1s XPS spectra of materials (Figure 4c) show an asymmetric peak with a shoulder, and the deconvolution of this peak reveals the presence of two different binding energies (531.3 eV e 532.7 eV) related to the oxygen present in SnO_2 and OH^- groups adsorbed on the surface, respectively.[48,49] $SnO_2/Au\_150\,°C$ showed two Au peaks, 4f5/2 and 4f7/2, with binding energy at 83.6 and 87.0 eV, respectively (Figure 4d).

CO₂ photoreduction (CO₂PR)

A semiconductor's ability to catalyze reactions is highly dependent to the presence and type of functional groups that are present on its surface. Among these, hydroxyls play a crucial role. In this sense, these groups were identified using the NIR analysis (Figure 5). Two main bands are associated with the adsorption of OH and H_2O groups, located at 5170 cm^{-1} and 6890 cm^{-1}, respectively. Specifically, the band at approximately 5170 cm^{-1} is related to the combination ($\delta + v3$) of the bending (δ) and asymmetric stretching ($v3$) vibrational modes of water molecules physisorbed on the solid surface. The band at 6890 cm^{-1} is related to the combination ($v1 + v3$) of the symmetrical ($v1$) and asymmetric ($v3$) stretching vibrational modes of OH bonds in H_2O molecules.[39,50,51]
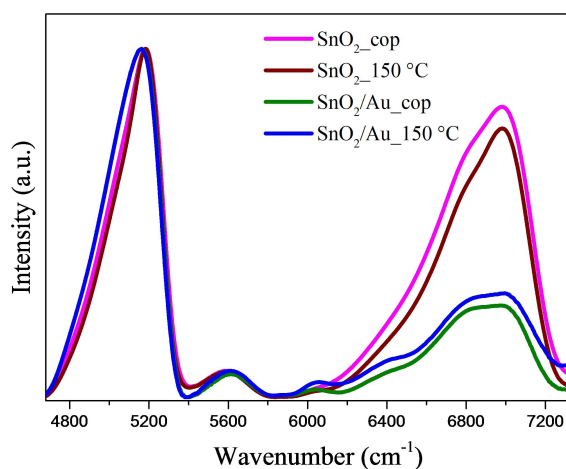
The band attributed to crystalline water contains contributions from a variety of water molecule vibration modes, including those linked to an active hydrogen bond (S1), two active hydrogen bonds (S2), and finally, the polymeric chain of water molecules that are connected (Sn) (Figure S5). Since there is a visible difference between these groups among the samples, it is possible to confirm the tendency of decreasing the content of hydroxyl groups with calcination and with the addition of gold on the SnO_2 surface, respectively, through the total area corresponding to the stretching vibrational modes of OH bonds (6890 cm^{-1}) (Table 2).

The proportion of surface hydroxyl groups has a slight drop with calcination, while this drop is intensely accentuated with the impregnation of gold nanoparticles on the SnO_2 surface. The crystalline water content is practically the same for all samples since the same coprecipitation process obtains them. As these groups are directly associated with photoactivity, as observed in previous works,[39] the decrease in these surface hydroxyl groups resulted in a lower photocatalytic response (Figure 5).

A complementary analysis in the quantification of surface water groups was performed through the normalization of the band referring to the O—Sn—O stretching mode (~581 cm^{-1})[36,37] of the infrared spectrum (Figure 6). In this sense, the relationship between the bands of H_2O (1630–1640 cm^{-1}) and OH (2500–3500 cm^{-1})[52] will vary depending on the amount of water molecules, which can be easily verified through the quotient between the H_2O/O—Sn—O and OH/O—Sn—O areas, respectively (Table 3).

According to the results obtained, the contribution of OH groups to SnO_2_cop is about 8 times higher than samples calcined at 150°C and SnO_2/Au_cop, respectively. The calcination process eliminates weakly bind water molecules, corroborating the observations obtained. Decoration of SnO_2 with gold nanoparticles also led to a decrease in these surface groups. Thus, the gold amount at SnO_2 surface may have reduced the number of active sites for CO_2 adsorption, consequently causing a deleterious effect on CO_2 photoreduction. All these data corroborate the NIR spectrum observations.
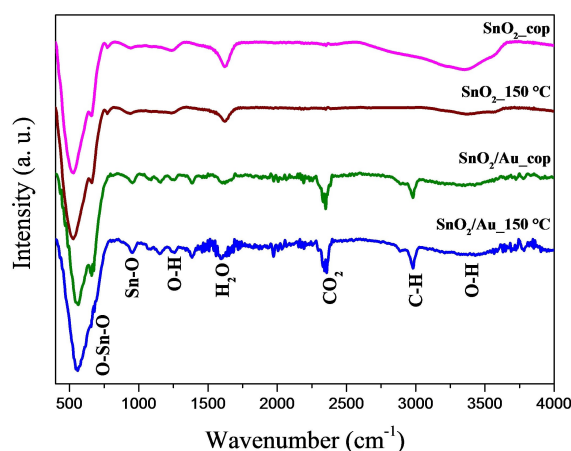

Figure 5. Near-infrared spectrum (NIR) of the SnO_2_cop and SnO_2/Au and calcined at 150°C.

Table 2. The total area of bands related to water adsorption on the SnO_2 surface.

Material	Vibration mode of the water molecules in the NIR spectrum	
	Physisorbed H_2O molecule [~5170 cm^{-1}]	Surface hydroxyl groups [~6980 cm^{-1}]
SnO_2_cop	305.36	443.45
$SnO_2\_150\,°C$	283.01	390.43
SnO_2/Au_cop	332.59	140.03
$SnO_2/Au\_150\,°C$	328.18	134.88

Figure 6. FTIR spectra of the SnO_2 cop, SnO_2/Au, and calcined at 150°C.

ChemCatChem

Research Article
doi.org/10.1002/cctc.202201534

Chemistry
Europe
European Chemical
Societies Publishing

Table 3. Absolute areas (A) for O–Sn–O, H_2O, and OH bands of the FTIR spectrum.

Material	A_{O-Sn-O} (581 cm^{-1})	A_{H2O} (1630–1640 cm^{-1})	A_{OH} (2500–3500 cm^{-1})	A_{H2O}/A_{O-Sn-O}	A_{OH}/A_{O-Sn-O}
SnO$_2$_cop	191.58	13.78	122.31	0.07	0.64
SnO$_2$_150°C	194.04	7.99	16.13	0.04	0.08
SnO$_2$/Au_cop	195.02	6.82	17.81	0.03	0.09
SnO$_2$/Au_150°C	193.14	11.07	24.78	0.06	0.13

As highlighted earlier, it is known that SnO_2 has some intrinsic characteristics that do not make it a good candidate for photocatalytic applications. On the other hand, the experimental findings corroborate earlier findings and show that SnO_2 is a photocatalytic material and that its activity and selectivity in the gas phase CO_2 photoreduction process are determined by the OH groups present in the semiconductor structure.

The results demonstrate the formation of four products in the CO_2 photoreduction process in the gas phase, including ethane (C_2H_6), ethylene (C_2H_4), carbon monoxide (CO), and methane (CH_4), after 6 hours of reaction (Figure 7). It is worth mentioning that only CH_4 and CO were detected in our experimental system without a catalyst (blank test), and these values were taken out of the data that were presented. The products formed are obtained by the CO_2 photocatalytic reduction instead of decomposing some precursor or contaminant, as no gaseous products could be seen without CO_2 under a N_2 atmosphere.

The amount of CH_4 generated after 6 h of reaction was 31.1, 12.5, 15.1, and 7.93 µmol g^{-1} for the materials SnO$_2$-cop, SnO$_2$_150°C, SnO$_2$/Au_cop and SnO$_2$/Au_cop_150°C respectively, with a production of about 2 to 4 times greater than SnO$_2$_cop compared to gold-impregnated and heat-treated materials (Figure 7a). Regarding the production of CO and C_2H_4, the SnO$_2$-cop showed similar activity to the annealed material at 150°C, and superior to materials with gold nanoparticles (Figure 7b

and c). However, SnO$_2$/Au_150°C presented higher C_2H_6 production, approximately 0.71 µmol/g (Figure 7d).

These findings demonstrate that the heat treatment and gold nanoparticles on the SnO_2 surface were deleterious to the CO_2 photoreduction process, reducing the quantity of electrons transported by half (Table S1). These findings support the theory that the availability of surface hydroxyl groups on SnO_2, which are necessary for CO_2 photoreduction, is influenced by the heating process and the impregnation of SnO_2 with gold. Therefore, we can observe that even with a decrease in the electron-hole pair recombination rate and good absorption of ultraviolet radiation after the composite formation, the affinity of the CO_2 molecules with the catalyst's surface may have been the factor that exerted more significant influence on photocatalytic activity.

It is indisputable that photoactivity is dependent not only on the catalyst's structural, morphological, and optical characteristics but also on the reaction conditions to which the material will be subjected. During the CO_2 photoreduction, while the photogenerated electrons will drive reduction reactions, the holes will drive oxidation reactions. Therefore, CO_2 will be reduced by electrons, giving rise to $^\bullet CO_2^-$ radicals, and water will be oxidized, producing hydrogen ions (H$^+$) and hydroxyl radicals ($^\bullet OH$), according to the equation below (Eq. 1):

$$H_2O + h^+ \rightarrow {}^\bullet OH + H^+ \tag{1}$$
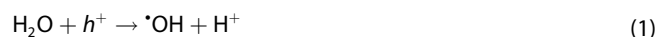
These radicals, in turn, can undergo further oxidation, leading to the formation of oxygen (O_2) and hydrogen ions (H$^+$) (Eq. 2):

$$H_2O + h^+ \rightarrow {}^\bullet OH + H^+ + e^- + H_2O \rightarrow O_2 + H^+ \tag{2}$$
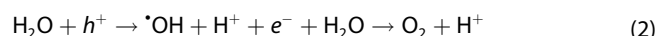
The $^\bullet H$ radicals can originate from the proton reduction of carbon radicals attached to the catalyst surface. These $^\bullet H$ radicals can lead to the formation of different intermediates, such as $^\bullet CH_2$ and $^\bullet CH_3$, which lead to the production of CH_4 and other hydrocarbons like C_2H_6, C_3H_6 and C_2H_4.[10,53,54]

Reactions conducted in the liquid phase favor the rapid hydrogenation of the reaction intermediates due to the high availability of hydrogen. In contrast, in the gas phase, deoxygenation is preferred, leading to carbon species that will later be reduced.[55] Thus, the synthesized materials' properties and the CO_2 photoreduction in the gas phase resulted in better selectivity for CH_4 (Figure S6). The formation of this product passes through the intermediate CO, and after consecutive reactions, it produces the $CH_3{}^\bullet$ radical, which, when combined
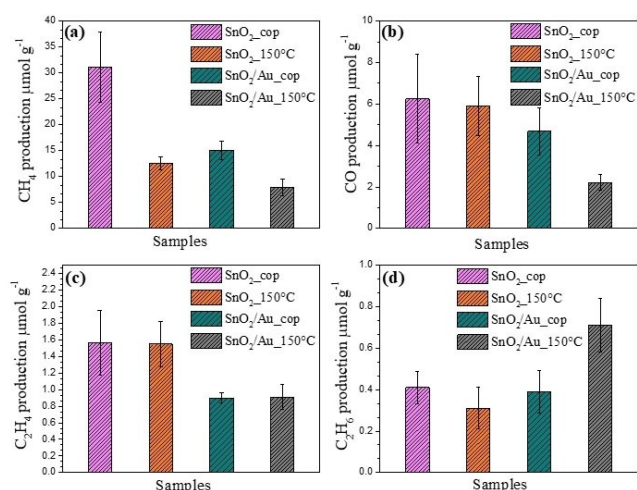

Figure 7. Products (a) methane, (b) carbon monoxide, (c) ethylene, and (d) ethane obtained during the CO_2 photoreduction in the gas phase ($CO_2 + H_2O$ steam) after 6 h of reaction using UV light at 15°C. Reaction conditions: batch reactor (14 mL working volume) and 10 mg of catalyst.

ChemCatChem

Research Article
doi.org/10.1002/cctc.202201534

Chemistry
Europe
European Chemical
Societies Publishing

with the H^+ from the water splitting, results in the formation of CH_4 (Eq. 3).[54,56]

$$CO_2 \rightarrow CO \rightarrow C^{\bullet} \rightarrow CH^{\bullet} \rightarrow CH_3^{\bullet} \rightarrow CH_4 \qquad (3)$$
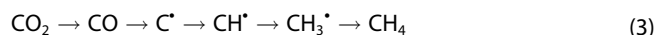
In gas-phase CO_2 photoreduction, C2 products, such as C_2H_4 and C_2H_6, have also been identified in addition to C1 products (CH_4 and CO). Surface hydroxyls played a significant role in the C—C coupling capacity, contributing to the formation of higher hydrocarbons through the dimerization process.[57] The basic Lewis characteristics of hydroxyls favor the adsorption of the CO_2 molecule, which in turn, has an acidic character. Dimerization results from successive reactions with different intermediates, forming longer hydrocarbons such as C_2H_4 and C_2H_6, as suggested by Figure 8. Gold nanoparticles formation at the SnO_2 surface replaces the hydroxyl groups; therefore, the photocatalytic activity is impaired.

The results obtained should be highlighted compared to other reports in the literature on CO_2 photoreduction using gas-phase systems, even for classical systems employing TiO_2. From the results presented in the Table 4, we can suggest that the materials used are promising photocatalytic agents for CO_2 conversion into hydrocarbons. Although not exhibiting the highest efficiency in some cases, as in the production of CO and CH_4, the prepared materials were more efficient in the production of higher hydrocarbons (C2+). Moreover, it is

important to note the simplicity and effectiveness of the system in this work compared to others, given the absence of sacrificial agents and the low power used by the irradiation source (only 18 W). Since the employed semiconductor does not exhibit characteristics that are conducive to CO_2 reduction, the results obtained must be highlighted because they demonstrated an important photocatalytic performance.

Given that gold nanoparticles are known to exhibit surface plasmonic resonance at wavelengths of about 550 nm, the identical gas-phase CO_2 photoreduction reaction was carried out using visible light (white LED). While the charge mediators responsible for photoactivity in UV radiation are the $Sn(OH)_4$ groups, in visible radiation, the surface plasmons of gold nanoparticles create a strong local electric field, resulting in selective photoactivity towards methane.[41,42,45] As seen in Figure 9, the yields are significantly lower under visible radiation than UV radiation, but the influence of gold on photoactivity is evident. While for the sample without heat treatment, the addition of gold nanoparticles, the selectivity for methane almost doubles. For samples calcined at 150 °C, this difference is nearly 10 times. This behavior demonstrates that the incident photons' energy matches the gold's surface plasmonic resonance, being excited electrons transferred to the CO_2 molecule, consequently increasing its photoreduction capacity (Figure 10).
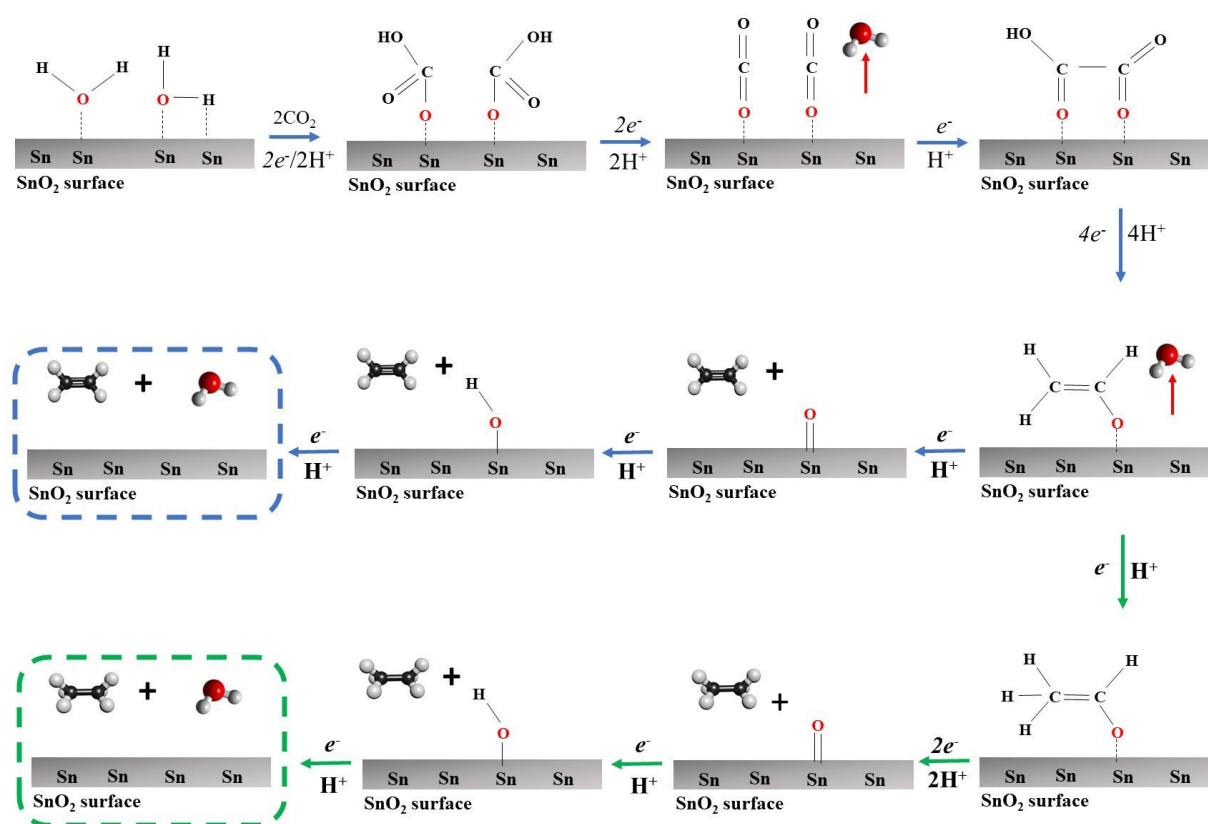

Figure 8. Schematic of the CO_2 reduction mechanism to C_2H_4 and C_2H_6. The oxygen atoms are shown in red, the hydrogen atoms in gray, and the carbon atoms in black.

Table 4. Comparison of the product formation rate during CO_2 photoreduction in gas-phase systems.

Catalyst	Light source	Reaction medium	Reactor type	Product formation rate [$\mu mol\,g^{-1}_{cat}\,h^{-1}$]				Ref.
				CH_4	CO	C_2H_4	C_2H_6	
TiO_2/Au	100 W Xe lamp (>320 nm)	$CO_2 + H_2O_{(vapor)}$	Gas phase	3.10	1.50	–	–	[58]
MgO–Pt–TiO_2	100 W Xe lamp (>320 nm)	$CO_2 + H_2O_{(vapor)}$	Gas phase	6.30	0.02	–	–	[58]
TiO_2/NrGO	400 W Xe lamp (>400 nm)	$CO_2 + H_2O_{(vapor)}$	Gas phase	–	50.0	–	–	[59]
In_2O_3	300 W Xe lamp (>420 nm)	$CO_2 + H_2O_{(vapor)}$	Gas phase	27.19	8.25	–	–	[60]
Ce–TiO_2/SBA	450 W Xe lamp	$CO_2 + H_2O_{(vapor)}$	Gas phase	2.00	1.88	–	–	[61]
TiO_2/Ag_3PO_4	300 W Xe lamp	$CO_2 + H_2O_{(vapor)}$	Gas phase	–	24.94	–	–	[62]
(Au, Cu)/TiO_2	1000 W Xe lamp	$CO_2 + H_2O_{(vapor)}$	Gas phase	44.00	–	–	–	[63]
Cu_3SnS_4	100 W Xe lamp	$CO_2 + H_2O_{(vapor)}$	Gas phase	14.20	8.40	–	–	[64]
RT-Cu	100 W Xe lamp	$CO_2 + H_2O_{(vapor)}$	Gas phase	0.01	–	–	–	[65]
TiO_2/SBA	120 W Hg lamp	$CO_2 + H_2O_{(vapor)}$	Gas phase	49.75	–	28.93	42.81	[66]
CuO_x@p-ZnO	300 W Xe lamp (>320 nm)	$CO_2 + H_2O_{(vapor)}$ + TEA*	Gas phase	17.90	27.30	22.30	–	[67]
SnO_2_cop	18 W – UVC	$CO_2 + H_2O_{(vapor)}$	Gas phase	5.18	1.04	0.27	0.07	This work
SnO_2/Au_cop	18 W – UVC	$CO_2 + H_2O_{(vapor)}$	Gas phase	2.52	0.78	0.15	0.07	This work

*TEA = triethylamine

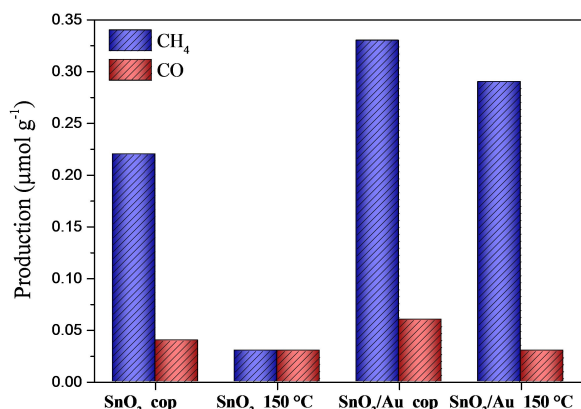**Figure 9.** CO_2 photoreduction in the gas phase ($CO_2 + H_2O$ steam) after 6 h of reaction under visible radiation at 15 °C. Reaction conditions: batch reactor (14 mL working volume) and 10 mg of catalyst.

Figure 10. Scheme of surface plasmon resonance of gold nanoparticles on the surface of SnO_2 and its influence on CO_2 photoreduction.

It is important to note that for SnO_2/Au system, the plasmonic effect is not significant when compared to the water bonding state effect, showing that this assumption (e.g., the role of plasmonic metals) could not be assumed as universal for different photocatalysts. In other words, it shows that the semiconductor acts as a photocatalyst rather than a simple support of plasmonic particles, which would be regarded as the active sites in these other mentioned systems.
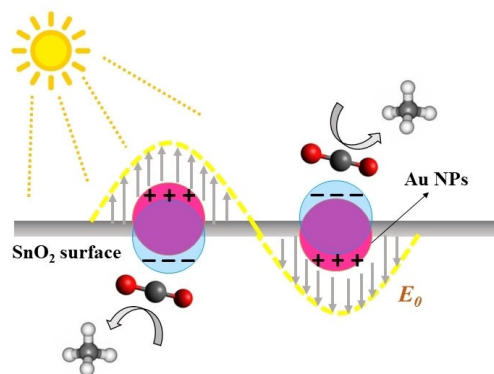
Conclusion

The SnO_2 nanoparticles obtained by coprecipitation showed high performance during CO_2 photoreduction in the gas phase, with high selectivity to methane ($\sim 90\%$ for SnO_2_cop). Although this semiconductor is recognized as having an unfavorable band structure for photocatalytic applications, the surface hydroxyl groups play a crucial role in the adsorption of the CO_2 molecule and, consequently, in its reduction process. Heat treatment and gold impregnation on the surface of this catalyst were deleterious during the reaction under UV irradiation since they decreased the availability of surface hydroxyls (starting from $\sim 30\ \mu mol\,g^{-1}$ in SnO_2_cop, with a drop of 59.81% and 51.45% in CH_4 production for SnO_2_150 °C and SnO_2/Au_cop, respectively). Under visible radiation (white LED),

the collective oscillation of electrons during the plasmonic resonance of the gold nanoparticles may have favored the adsorption of CO_2 molecules, leading to their reduction to CH_4 (0.33 µmol g^{-1} for SnO_2/Au_cop and 0.29 µmol g^{-1} for SnO_2/Au_150 °C) and CO (0.06 µmol g^{-1} for SnO_2/Au_cop and 0.03 µmol g^{-1} for SnO_2/Au_150 °C). These values evidenced that the plasmonic effect attributed to Au nanoparticles can not be considered the responsible for the photoactivity, and that SnO_2 is not acting as a catalyst support but the actual photocatalyst. Thus, under UV radiation, CO_2 photoreduction occurs by the charge mediators Sn(OH)$_4$, while under visible radiation, photoreduction results from the surface plasmonic resonance of gold on the SnO_2 surface. Therefore, these results demonstrate that SnO_2 is valuable for CO_2 photoreduction reactions, being its surface characteristics critical for the activity.

Experimental Section

Catalysts preparation

SnO_2 nanoparticles were synthesized according to Torres et al. (2020) with some modifications.[39] Typically, 100 mL of anhydrous ethanol (99.5 % purity, Dynamics) was used as the dispersing medium for 0.5 g of SnCl$_2$.2H$_2$O (Sigma-Aldrich). The suspension was stirred overnight after the addition of 22 mL of distilled water at room temperature. The resulting suspension was washed by centrifugation (8000×g, 10 min, 25 °C) with MiliQ water and ethanol to remove excess chlorine and dried at 50 °C overnight. This material was named SnO_2_cop. Finally, the co-prepared samples were calcined at 150 °C for 3 h. Gold nanoparticles on the SnO_2 surface were obtained by reducing a solution of chloroauric acid (HAuCl$_4$, Exodo) with a concentrated solution of sodium borohydride (NaBH$_4$, Aldrich, ≥ 96 %). For this, in the suspension of SnCl$_2$.2H$_2$O in water and ethanol, a solution of 1 % HAuCl$_4$ was added to obtain a proportion of SnO_2/Au 1 % (wt%), which was kept under stirring for 30 min for complete homogenization. The sodium borohydride solution was added dropwise to the previously prepared suspension under constant stirring. The obtained material was washed by centrifugation (8000×g, 10 min, 25 °C) with MiliQ water and ethanol and then lyophilized. This sample was denoted SnO_2/Au_cop, while the calcined (for 3 h) was called SnO_2/Au_150 °C.

Characterization

Elemental analysis, diffuse reflectance, Raman, and X-ray photoelectron spectroscopy, together with X-ray diffractometry, scanning and high-resolution transmission electron microscopy, were used to determine the characteristics of the synthesized materials. X-ray fluorescence was used to calculate the quantity of gold on the SnO_2 surface. In the Supplementary Material, the procedures are described in further detail.

CO_2 photoreduction reaction (CO_2PR)

Using a technique that has been previously reported, the CO_2 photoreduction was carried out using 10 mg of catalyst that was placed as a film on a glass substrate.[39] The catalysts were exposed to UV light (18 W/mercury lamp) in a gas-solid system for 6 hours at 15 °C and air pressure. Gas chromatography was used to identify the products that were collected. The Supplementary Material

contains more information about the CO_2 photoreduction that was done.

Conflict of Interest

The authors declare no conflict of interest.
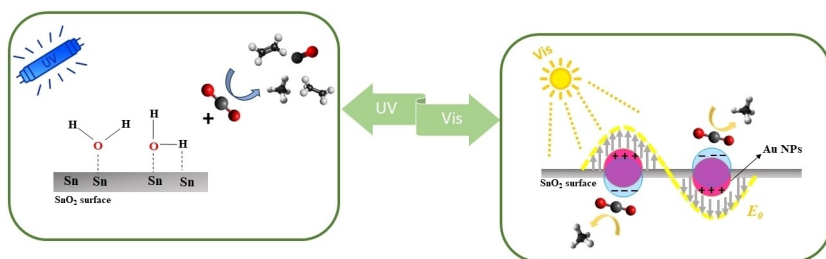
Data Availability Statement

The data that support the findings of this study are available from the corresponding author upon reasonable request.

Keywords: Artificial photosynthesis · Noble metals · Surface features · Selectivity · Plasmonic resonance

[1] E. Masood, J. Tollefson, *Nature* **2021**, *599*, 355–356.
[2] G. Vaidyanathan, *Nature* **2021**, DOI 10.1038/d41586-021-03044-x.
[3] I. Ganesh, *Renewable Sustainable Energy Rev.* **2016**, *59*, 1269–1297.
[4] H. Liu, X. Meng, W. Yang, G. Zhao, D. He, J. Ye, *Chin. J. Catal.* **2021**, *42*, 1976–1982.
[5] S. Nitopi, E. Bertheussen, S. B. Scott, X. Liu, A. K. Engstfeld, S. Horch, B. Seger, I. E. L. Stephens, K. Chan, C. Hahn, J. K. Nørskov, T. F. Jaramillo, I. Chorkendorff, *Chem. Rev.* **2019**, *119*, 7610–7672.
[6] V. Kumaravel, J. Bartlett, S. C. Pillai, *ACS Energy Lett.* **2020**, *5*, 486–519.
[7] A. E. Nogueira, G. T. S. T. Silva, J. A. Oliveira, O. F. Lopes, J. A. Torres, M. Carmo, C. Ribeiro, *ACS Appl. Energ. Mater.* **2020**, *3*, 7629–7636.
[8] J. Y. Y. Loh, N. P. Kherani, G. A. Ozin, *Nat. Sustain.* **2021**, *4*, 466–473.
[9] N. Mac Dowell, P. S. Fennell, N. Shah, G. C. Maitland, *Nat. Clim. Change* **2017**, *7*, 243–249.
[10] D. Ješić, D. Lašič Jurković, A. Pohar, L. Suhadolnik, B. Likozar, *Chem. Eng. J.* **2021**, *407*, 126799.
[11] Ž. Kovačič, B. Likozar, M. Huš, *ACS Catal.* **2020**, *10*, 14984–15007.
[12] M. Kandasamy, A. Seetharaman, D. Sivasubramanian, A. Nithya, K. Jothivenkatachalam, N. Maheswari, M. Gopalan, S. Dillibabu, A. Eftekhari, *ACS Appl. Nano Mater.* **2018**, *1*, 5823–5836.
[13] Y. Wang, M. Peng, J. Zhang, Z. Zhang, J. An, S. Du, H. An, F. Fan, X. Liu, P. Zhai, D. Ma, F. Wang, *Nat. Commun.* **2018**, *9*, DOI 10.1038/s41467-018-07593-0.

ChemCatChem

Research Article
doi.org/10.1002/cctc.202201534

Chemistry Europe
European Chemical
Societies Publishing

[14] S. Mardiana, N. J. Azhari, T. Ilmi, G. T. M. Kadja, *Fuel* **2022**, *309*, DOI 10.1016/j.fuel.2021.122119.

[15] S. Shao, J. Liu, G. Portale, H. H. Fang, G. R. Blake, G. H. ten Brink, L. J. A. Koster, M. A. Loi, *Adv. Energy Mater.* **2018**, *8*, 1702019.

[16] K. Nishimura, D. Hirotani, M. A. Kamarudin, Q. Shen, T. Toyoda, S. Iikubo, T. Minemoto, K. Yoshino, S. Hayase, *ACS Appl. Mater. Interfaces* **2019**, *11*, 31105–31110.

[17] Q. Cai, Y. Zhang, C. Liang, P. Li, H. Gu, X. Liu, J. Wang, Z. Shentu, J. Fan, G. Shao, *Electrochim. Acta* **2018**, *261*, 227–235.

[18] W. Zhang, Q. Li, C. Wang, J. Ma, H. Peng, Y. Wen, H. Fan, *Ceram. Int.* **2019**, *45*, 20566–20574.

[19] E. Pargoletti, U. H. Hossain, I. Di Bernardo, H. Chen, T. Tran-Phu, G. L. Chiarello, J. Lipton-Duffin, V. Pifferi, A. Tricoli, G. Cappelletti, *ACS Appl. Mater. Interfaces* **2020**, *12*, 39549–39560.

[20] L. Liang, H. Lv, X. L. Shi, Z. Liu, G. Chen, Z. G. Chen, G. Sun, *Mater. Horiz.* **2021**, *8*, 2750–2760.

[21] X. Ding, D. Liang, X. Ai, H. Zhao, N. Zhang, X. Chen, J. Xu, H. Yang, *ACS Appl. Energ. Mater.* **2021**, *4*, 2741–2750.

[22] J. Liu, D. Xie, X. Xu, L. Jiang, R. Si, W. Shi, P. Cheng, *Nat. Commun.* **2021**, *12*, DOI 10.1038/s41467-021-23335-1.

[23] Y. Yan, Y. Liu, Y. Zhang, C. Qin, H. Yu, Z. Bakenov, Z. Wang, *J. Colloid Interface Sci.* **2021**, *602*, 563–572.

[24] G. T. S. T. da Silva, O. F. Lopes, E. H. Dias, J. A. Torres, A. E. Nogueira, L. A. Faustino, F. S. Prado, A. O. T. Patrocínio, C. Ribeiro, *Quím. Nova* **2021**, *44*, 963–981.

[25] E. Abdelkader, L. Nadjia, B. Naceur, B. Noureddine, *J. Alloys Compd.* **2016**, *679*, 408–419.

[26] A. H. Chowdhury, A. Das, S. Riyajuddin, K. Ghosh, S. M. Islam, *Catal. Sci. Technol.* **2019**, *9*, 6566–6569.

[27] J. A. Torres, G. T. S. T. Da Silva, F. Barbosa de Freitas Silva, C. Ribeiro, *ChemPhysChem* **2020**, *21*, 2392–2396.

[28] N. Chen, B. Liu, P. Zhang, C. Wang, Y. Du, W. Chang, W. Hong, *Inorg. Chem. Commun.* **2021**, *132*, 108848.

[29] Z. Chen, T. Fan, Y. Q. Zhang, J. Xiao, M. Gao, N. Duan, J. Zhang, J. Li, Q. Liu, X. Yi, J. L. Luo, *Appl. Catal. B* **2020**, *261*, 118243.

[30] L. Soussi, T. Garmim, O. Karzazi, A. Rmili, A. El Bachiri, A. Louardi, H. Erguig, *Surf. Interfaces* **2020**, *19*, 100467.

[31] J. A. Torres, J. C. da Cruz, A. E. Nogueira, G. T. S. T. da Silva, J. A. de Oliveira, C. Ribeiro, *J. Environ. Chem. Eng.* **2022**, *10*, 107291.

[32] F. Li, L. Chen, G. P. Knowles, D. R. MacFarlane, J. Zhang, *Angew. Chem. Int. Ed.* **2017**, *56*, 505–509; *Angew. Chem.* **2017**, *129*, 520–524.

[33] A. Diéguez, A. Romano-Rodríguez, A. Vilà, J. R. Morante, *J. Appl. Phys.* **2001**, *90*, 1550–1557.

[34] K. Pavithra, S. M. S. Kumar, *Catal. Sci. Technol.* **2020**, *10*, 1311–1322.

[35] F. Ospitali, C. Chiavari, C. Martini, E. Bernardi, F. Passarini, L. Robbiola, *J. Raman Spectrosc.* **2012**, *43*, 1596–1603.

[36] R. Shyamala, L. Gomathi Devi, *Chem. Phys. Lett.* **2020**, *748*, 137385.

[37] B. Babu, I. Neelakanta Reddy, K. Yoo, D. Kim, J. Shim, *Mater. Lett.* **2018**, *221*, 211–215.

[38] V. R. De Mendonça, O. F. Lopes, R. P. Fregonesi, T. R. Giraldi, C. Ribeiro, *Appl. Surf. Sci.* **2014**, *298*, 182–191.

[39] J. A. Torres, G. T. S. T. da Silva, F. Barbosa de Freitas Silva, C. Ribeiro, *ChemPhysChem* **2020**, *21*, 2392–2396.

[40] H. Wang, Y. Wang, L. Guo, X. Zhang, C. Ribeiro, T. He, *Chin. J. Catal.* **2020**, *41*, 131–139.

[41] L. Collado, A. Reynal, J. M. Coronado, D. P. Serrano, J. R. Durrant, V. A. De la Peña O'Shea, *Appl. Catal. B* **2015**, *178*, 177–185.

[42] B. Kholikov, J. Hussain, H. Zeng, *Inorg. Chem. Commun.* **2021**, *131*, 108787.

[43] H. Yang, Y. Huang, J. Deng, Y. Wu, N. Han, C. Zha, L. Li, Y. Li, *J. Energy Chem.* **2019**, *37*, 93–96.

[44] A. Zada, M. Humayun, F. Raziq, X. Zhang, Y. Qu, L. Bai, C. Qin, L. Jing, H. Fu, *Adv. Energy Mater.* **2016**, *6*, 201601190.

[45] D. Barman, S. Paul, S. Ghosh, S. K. De, *ACS Appl. Nano Mater.* **2019**, *2*, 5009–5019.

[46] D. Fang, F. He, J. Xie, L. Xue, *J. Wuhan Univ. Technol. Mater. Sci. Ed.* **2020**, *35*, 711–718.

[47] A. Sharma, S. Arya, D. Chauhan, P. R. Solanki, S. Khajuria, A. Khosla, *J. Mater. Res. Technol.* **2020**, *9*, 14321–14337.

[48] G. A. S. Alves, H. A. Centurion, J. R. Sambrano, M. M. Ferrer, R. V. Gonçalves, *ACS Appl. Energ. Mater.* **2021**, *4*, 671–679.

[49] F. A. Akgul, C. Gumus, A. O. Er, A. H. Farha, G. Akgul, Y. Ufuktepe, Z. Liu, *J. Alloys Compd.* **2013**, *579*, 50–56.

[50] F. Silva, G. da Silva, J. Torres, C. Ribeiro, *J. Braz. Chem. Soc.* **2022**, 20220009.

[51] D. A. Popescu, J. M. Herrmann, A. Ensuque, F. Bozon-Verduraz, *Phys. Chem. Chem. Phys.* **2001**, *3*, 2522–2530.

[52] G. Elango, S. M. Roopan, *J. Photochem. Photobiol. B* **2016**, *155*, 34–38.

[53] M. Wang, Q. Zhang, Q. Xie, L. Wan, Y. Zhao, X. Zhang, J. Luo, *Nanoscale* **2020**, *12*, 17013–17019.

[54] D. Ren, J. Fong, B. S. Yeo, *Nat. Commun.* **2018**, *9*, DOI 10.1038/s41467-018-03286-w.

[55] A. Olivo, E. Ghedini, M. Signoretto, M. Compagnoni, I. Rossetti, *Energies* **2017**, *10*, 1394.

[56] E. Karamian, S. Sharifnia, *J. CO2 Util.* **2016**, *16*, 194–203.

[57] W. Zhu, B. M. Tackett, J. G. Chen, F. Jiao, *Top. Curr. Chem.* **2018**, *376*, DOI 10.1007/s41061-018-0220-5.

[58] S. Xie, Y. Wang, Q. Zhang, W. Deng, Y. Wang, *ACS Catal.* **2014**, *4*, 3644–3653.

[59] L. Y. Lin, Y. Nie, S. Kavadiya, T. Soundappan, P. Biswas, *Chem. Eng. J.* **2017**, *316*, 449–460.

[60] B. Hu, Q. Guo, K. Wang, X. Wang, *J. Mater. Sci. Mater. Electron.* **2019**, *30*, 7950–7962.

[61] C. Zhao, L. Liu, Q. Zhang, J. Wang, Y. Li, *Catal. Sci. Technol.* **2012**, *2*, 2558–2568.

[62] F. Qi, H. Li, Z. Yang, J. Zhao, Y. Hu, H. Liu, *Asia-Pacific J. Chem. Eng.* **2020**, *15*, e2499.

[63] S. Neatu, J. A. Maciá-Agulló, P. Concepciòn, H. Garcia, *J. Am. Chem. Soc.* **2014**, *136*, 15969–15976.

[64] N. Sharma, T. Das, S. Kumar, R. Bhosale, M. Kabir, S. Ogale, *ACS Appl. Energ. Mater.* **2019**, *2*, 5677–5685.

[65] S. Ali, J. Lee, H. Kim, Y. Hwang, A. Razzaq, J. W. Jung, C. H. Cho, S. Il In, *Appl. Catal. B* **2020**, *279*, 119344.

[66] C. C. Yang, J. Vernimmen, V. Meynen, P. Cool, G. Mul, *J. Catal.* **2011**, *284*, 1–8.

[67] W. Wang, C. Deng, S. Xie, Y. Li, W. Zhang, H. Sheng, C. Chen, J. Zhao, *J. Am. Chem. Soc.* **2021**, *143*, 2984–2993.

RESEARCH ARTICLE

Dra. J. A. Torres, Dr. A. E. Nogueira, Dr. G. T. S. T. da Silva, Dr. C. Ribeiro*

1 – 10

The Effect of SnO$_2$ Surface Properties on CO$_2$ Photoreduction to Higher Hydrocarbons

CO$_2$ photoreduction using SnO$_2$ under UV radiation lead to CO, C$_2$H$_4$, and C$_2$H$_6$, with higher selectivity for CH$_4$. The same reaction under visible light using Au-decorated SnO$_2$ produces CH$_4$ and a smaller amount of CO but in much lower yields.

Although the SnO$_2$ band structure does not indicate a good semiconductor for CO$_2$ reduction, its surface characteristics are responsible for its catalytic activity, and it does not act as a simple support for other catalysts, as plasmonic metals.